LJMU Research Online

Al-Mahdy, A, Kotadia, H, Sharp, MC, Opoz, T, Mullett, J and Ahuir Torres, JI

 Effect of Surface Roughness on the Surface Texturing of 316l Stainless Steel by Nanosecond Pulsed Laser

http://researchonline.ljmu.ac.uk/id/eprint/18355/

Article

Check for
updates

Effect of Surface Roughness on the Surface Texturing of 316 l Stainless Steel by Nanosecond Pulsed Laser

A. Al-Mahdy[1] · H. R. Kotadia[2] · M. C. Sharp[1] · T. T. Opoz[1] · J. Mullett[2] ·
J. I. Ahuir-Torres[1]

Abstract

Stainless steel 316L is an austenitic alloy that is widely used in varying industries due to its outstanding corrosion resistance, high strength, and ductility properties. However, the wear and friction resistance properties are low. Laser surface texturing can improve the wear and friction resistance of the material via the functionalisation of the surface. The laser surface texturing efficiency and the texture quality are defined by the material's surface properties and laser parameters. The surface roughness is an important material property having an effect on laser surface texturing. This paper reports on a study of the material's surface roughness influence on the texturing of 316L stainless steel with 1064 nm nanosecond pulsed laser. Single pulse shots were employed to avoid the topographic influence of the previous laser shots. The surface shape and the topography of the textures were assessed using optical microscopy and profilometry. It was observed that the textures produced were dimples of U-type and sombrero-like type geometries depending on surface roughness and pulse energy. The overall quality of the texture shape was better for smoother surfaces. The energy fluence necessary to generate textures is lower on surfaces of lower roughness than surfaces with high roughness. The surface at 24 nm of average roughness is the best surface for creating deep textures. The ablation mechanisms associated with high pulse energy, including plasma shielding, are produced at lower pulse energies for the 100 nm roughness, compared with other roughness samples.

Keywords Surface Roughness · Laser Surface Texturing · Nanosecond Pulsed Laser · Single Pulse · Energy Fluence Threshold · Dimples and Energy Depth Penetration

✉ J. I. Ahuir-Torres
   j.i.ahuirtorres@ljmu.ac.uk

1   General Engineering Research Institute, Faculty of Engineering and Technology, Liverpool John Moores University, Byrom Street, Liverpool L3 3AF, UK

2   School of Engineering, Faculty of Engineering and Technology, Liverpool John Moores University, Byrom Street, Liverpool L3 3AF, UK

 Springer

Nomenclature

Acronyms, Abbreviations, Initialisms:

316L SS	AISI 316L austenitic low carbon stainless steel
HAZ	Heat Affected Zone
IR	Infrared
LST	Laser Surface Texturing

Physical Quantities:

C_p	Specific Heat Capacity [J/(kg K)]
d	Dimple diameter [m]
d_{o-a}	Experimental focused laser beam diameter for ablation process [m]
d_{o-m}	Experimental focused laser beam diameter for melting process [m]
$d_{o(Theo)}$	Theoretical focused laser beam diameter [m]
d_t	Distance between pulse [m]
De	Dimple depth [m]
D_R	Laser beam raw diameter [m]
E_p	Pulse energy [J]
E_{pm}	Maximum pulse energy [J]
E_{th-da}	Experimental minimum pulse energy to create a dimple with visible depth [J]
E_{th-m}	Minimum experimental energy threshold for melting process [J]
E_{th-sa}	Minimum experimental laser energy to ablate the surface [J]
FL	Focal length [m]
l	Energy depth penetration [m]
l_{Theo}	Theoretical energy depth penetration [m]
M^2	Beam quality factor
N	Pulse number per shot
P_{ave}	Average power [W]
P_m	Maximum power [W]
PRF	Pulse Rate Frequency [Hz]
R	Reflectivity
S_a	Surface average roughness [m]
SR	Laser beam scan rate [m/s]
T_m	Melting Temperature [K]
T_e	Vaporisation Temperature [K]
T_o	Standard Temperature [K]
W	Dimple width [m]
α	Absorption coefficient [m/s]
β	Thermal conductivity [W/(m K)]
ΔH_m	Melting Enthalpy [J/kg]
ΔH_e	Evaporation Enthalpy [J/kg]
ζ	Geometrical factor
κ	Thermal diffusivity [m.^{2}/s]
λ	Wavelength [m]
ρ	Density [kg/m.^{3}]

τ	Pulse length [s]
φ_{th-da}	Minimum fluence energy to create a dimple with visible depth [J/m.^{2}]
φ_{th-m}	Minimum fluence energy threshold for the melting process [J/m.^{2}]
φ_{th-sa},	Minimum laser energy fluence to ablate the surface [J/m.2]
φ_{Theo-m}	Theoretical melting energy fluence [J/m.^{2}]
$\varphi_{th(Theo-e)}$,	Theoretical ablation fluence threshold [J/m.2

Introducton

AISI 316L austenitic low carbon stainless steel (316L SS) is a widely used stainless steel that is employed in many industries such as automotive, aerospace, marine, energetic, petrol-chemical, biomedical and others. This is due to its high corrosion resistance, good temperature resistance, acceptable biocompatibility, nonmagnetic and excellent mechanical properties (strength and ductility) [1–3]. This stainless steel nevertheless possesses a poor wear and friction resistance that restricts its use in the number of applications [3]. Surface texturing in combination with lubricants can be the solution to these latter problems. This is due to the fact that the textures can increase the lubricant lifetime because of their lubricant reservoir function. The wear can also be reduced by the textures as these have a wear debris trap function [4–6]. In the case of the liquid lubricant, the textures can furthermore decrease the coefficient of friction, and as a result of this can alter the hydrodynamics of the fluid [5, 7, 8].

Surface texturing is a powerful tool to functionalise the surface of a material. It can be carried out using several methods, such as ion beam, mechanical, etching, sand blasting, laser, plasma deposition and discharge electro machining. Laser Surface Texturing (LST) offers significant opportunities as a result of its exceptional properties such as environmentally friendly, precise, automation, and low cost of processing [7–9]. This technique can be conducted with several types of lasers that range from continuous wave lasers to femtosecond pulsed lasers, and from ultraviolet wavelengths to the mid-infrared. Near-infrared nanosecond pulsed lasers are widely employed for LST on metallic materials because of their small Heat Affected Zone (HAZ) in comparison to milli and microsecond pulsed lasers. They can offer, high peak power, good laser absorption and relatively low cost [9–11].

The traditional development field of LST is in the tribology of mechanical parts such as, gears, pistons, bearings, cylinders and others [12]. Eighteen years ago, Etsion [12] reviewed the application of LST on mechanical parts and associated basic research of LST in universities. The high reproducibility and precision of this technique is identified compared to other surface texturing methods. Subsequently, several researchers [13, 14] have investigated the influence of texture features (e.g. aspect ratio, shape, organisation and texture density) in the improvement of the wear and friction resistance, and the lasers (e.g. carbon dioxide, solid state, excimer and fibre) that can carry out these textures in a more efficient way. One of the challenges for LST in the 2010´s was the generation of the textures at a few micrometres or nanometres [14]. The creation of the laser induced periodic surface structures using polarised laser radiation was shown to produce the nano-textures, commonly

produced with pico and femtosecond pulsed laser [7, 15]. Micro-textures remain the main textures to improve the wear and friction resistance of the materials owing to their lubricant reservoir function. LST is carried out with a wide variety of lasers, from continuous wave through nanosecond pulsed laser to ultrashort pulsed (pico and femtosecond) [7, 16]. In the last decade, LST has also been employed in the biomedical industry to increase the biocompatibility of implants [15, 17–19]. The texturing at micro scale can improve the osseointegration of the implant while the laser induced periodic surface structures produce an antibacterial effect. For these reasons, lasers (e.g. polarised laser) that can create these nano-textures have become the focus of the biomedical industry. In the last few years, direct laser interference patterning is being developed in the biomedical field because of the generation of the patterns at varying scales in only one step [20].

The improvement of process efficiency is an important requirement for industrial applications. Efficiency of an industrial process is commonly defined by the power consumption, processing time and material requirements. Reducing these factor values increase the process performance [21–25]. In the case of the LST process, the efficiency can be defined by means of the laser beam-material interactions; energy fluence threshold and energy depth penetration. Energy fluence threshold is the minimum energy fluence necessary to carry out laser processing on the material (e.g. heating, melting, evaporation and ablation) [26]. Laser ablation is the principal process in laser surface texturing [27]. Low energy fluence thresholds allow texture creation at lower energy fluence values. This reduces power consumption. The energy fluence threshold can be classified as a surface parameter (energy fluence threshold to carry out a laser processing on surface). The energy depth penetration parameter mainly influences the laser processing into the material [28, 29]. The depth of textures is proportional to the energy depth penetration [29, 30]. High energy depth penetrations allow the generation of deeper textures using less energy fluence and pulse number [28, 29]. This provides a reduction in the power consumption (energy fluence) and process time (pulse number). It should be noted that an increase of the energy depth penetration relates to an increase in the energy fluence threshold, the energy fluence threshold being proportional to the energy depth penetration [31]. So, the efficiency of LST is higher at low energy fluence thresholds and at larger energy depth penetrations. Properties of LST are defined by the shape and size of the textures [7, 27, 32]. The laser processing and the texture features are defined by the laser parameters and the materials' properties [9, 33].

The roughness of the surface to be textured is an important factor that influences the shape and size of the texture and LST efficiency [34]. The optimum surface roughness for LST on metallic materials is the subject of discussion for researchers today. Several studies [26, 35] about LST on various metallic materials confirm that the increasing of surface roughness can improve the LST efficiency as this decreases the reflectivity of the material. High initial reflectivity of metallic alloys means that a significant part of the laser radiation is reflected, reducing the efficiency of the process. The reflectivity can be reduced via painting, coating deposition and surface roughening [35]. Other investigations [33, 36] have observed the opposite effect, where increased surface roughness decreased the efficiency of the laser process. This is owing to scattering effect of the roughened surface on the laser radiation

that can enlarge the area exposed by the laser radiation on the samples. This creates a reduction in the effective energy fluence that diminishes the LST efficiency. Another study [34] considers that the surface roughness influence can depend on the roughness level and the type of the metallic material. Currently, no study has given a satisfactory explanation about the roughness influence on the laser beam-material interactions.

For these reasons, a study about the influence of the surface roughness on single shot dimple LST of 316L SS with 1064 nm nanosecond laser pulses is reported in the present paper. Several single pulse shots were performed to produce separate dimples on SS316L surfaces with different average roughness to avoid the influence of the previous laser pulse surface topography on the LST efficiency. Laser beam-material interaction factors (energy depth penetration, melting and ablation, focused beam diameter, melting, surface and in-depth ablation energy fluence thresholds) were calculated and assessed to give a deeper understanding of the average roughness influence on the efficiency of LST.

Experimental Setup

Materials and Pre-treatment

Sample coupons were prepared from stainless steel AISI316L (SS316L) supplied by Columbus Stainless Ltd. The size of the samples was 50 mm by 50 mm by 0.8 mm thick. Chemical composition of the SS316L was provided by supplier and this is summarised in the Table 1. The physicochemical properties of the SS316L [27–29] can be observed in the Table 2.

Thermal diffusivity (κ) was calculated with Eq. 1 [26, 33, 40, 41].

$$\kappa = \frac{\beta}{\rho C_p} \tag{1}$$

Absorption coefficient (α) was estimated using Eq. 2 [38].

$$\alpha = \frac{4\pi k}{\lambda} \tag{2}$$

where, λ is the wavelength (1064 ± 5 nm).

Surfaces of the sample coupons were polished with various methods before laser processing (pre-treatment). This was carried out to get surfaces with dissimilar average roughness (S_a). The Sa values were measured using a *Bruker ContourGT optical profiler*. Two measurements were taken on five separate areas within each coupon. Assessment of the roughness was conducted with green light and at $27.5 \times$ magnification. Silicon carbide paper of grit 80P was used to obtain a surface with a S_a value of 360 ± 40 nm. A second surface was firstly polished with grit 80P abrasive paper and then with 400P silicon carbide paper. S_a of the second surface was 180 ± 30 nm. Third surface had a S_a of 100 ± 20 nm, which was achieved via a polishing process with subsequent abrasive papers that were grit 80P, grit 400P and grit 1200P. The

Table 1 SS316L chemical composition in weight percent (wt%)

Element	Fe	B	C	Co	Cr	Cu	Mn	Mo	N	Ni	P	S	Si
(%) wt	69.212	0.005	0.025	0.100	16.200	0.120	1.660	2.057	0.045	10.070	0.023	0.003	0.480

Table 2 SS316L Physical–chemical properties. *Value calculated using Eqs. (1), (2)

Property	Value
Specific Heat Capacity (C_p) [37]	0.498 J/(g K)
Thermal Conductivity (β) [37]	0.140 J/(K cm s)
Density (ρ) [37]	7.954 g/cm^3
Thermal Diffusivity* (κ)	0.035 cm^2/s
Absorption coefficient* (α)	0.047 nm^{-1}
Extinction coefficient (k) [38]	4.013
Melting Temperature (T_m) [37]	1700 K
Vaporisation Temperature (T_e) [37]	3090 K
Standard Temperature (T_o)	296 K
Melting Enthalpy (ΔH_m) [37]	1096 J/g
Evaporation Enthalpy (ΔH_e) [37]	2095 J/g
Reflectivity (R) [39]	55%

next sample was polished with grit 80P, grit 400P and grit 1200P silicon carbide paper and, polycrystalline diamond paste of 3 μm as the last polishing stage. This treatment produced a S_a value of 24 ± 10 nm. The final surface had a S_a value of 12 ± 8 nm that was generated through successive steps. First step was a grinding process with silicon carbide papers of grit 400P, grit 600P and grit 1200P. The next step was a sequential polishing via polycrystalline diamond pastes of 3 μm. The last step was mirror polishing employing a colloidal silica gel solution that was formed of 50% in volume of silica gel (0.04 μm of grain size) and 50% in volume of distilled water. All polishing consumables and items were provided by *Struers*. A cleaning process was conducted after each polishing treatment that consisted of first cleaning with commercial detergent and rinsing with fresh water, and then the surface was sprayed with isopropanol and, finally, a fast drying with a hot air dryer. Samples were named according to their S_a and therefore, these were called as 360 nm, 180 nm, 100 nm, 24 nm and 12 nm as can be seen in Table 3. Note, S_a was measured on ten areas with optical profilometer whose specifications will be detailed later.
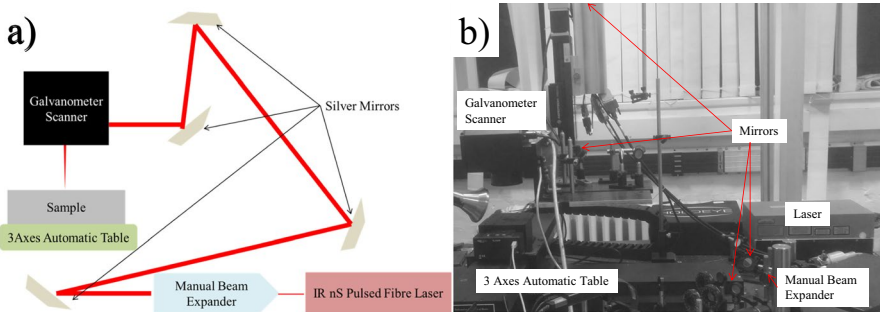
Laser Equipment and Parameters

The laser system used was formed of an infrared (IR) fibre laser, an optical system and a three axes automatic table. The IR fibre laser model was a *SPI Laser (UK) G3 20 W nanosecond pulsed fibre laser*. Optical system consisted of a manual 1064 nm beam expander (*Linos (Qioptiq) 2-8x*), a scanning galvanometer (*Nutfield Extreme-15-YAG*) controlled using *SAMLight v3.05* software (*SCAPS Gmbh*), a focal length of 100 mm (*Linos Ronar F-Theta focal lens)* and four silver mirrors (*Thorlab*). The three axes computer-controlled table was provided by *Aerotech Limited (UK)*. Figure 1 illustrates a schematic drawing of this equipment.

The laser has a wavelength (λ) 1064 ± 5 nm, and a near TEM$_{00}$ mode with beam quality factor $M^2 = 2.1$. The laser can work with several pulse lengths (τ) varying from 9 to 200 ns and at various Pulse Repetition Frequencies (*PRF*) that range from

Table 3 Summary of the samples and their pre-treatments

Name of the sample	Silicon carbide paper, diamond paste and colloidal silica gel dissolution used	S_a of the sample (nm)
360 nm	grit 80P	360 ± 40
180 nm	1. grit 80P	180 ± 30
	2. grit 400P	
100 nm	1. grit 80P	100 ± 20
	2. grit 400P	
	3. grit 1200P	
24 nm	1. grit 80P	24 ± 10
	2. grit 400P	
	3. grit 1200P	
	4. 3 µm diamond paste	
12 nm	1. grit 80P	12 ± 8
	2. grit 400P	
	3. grit 1200P	
	4. 3 µm diamond paste	
	5. 50% in volume of colloidal silica gel of 40 nm size	

Fig. 1 Laser equipment and experimental setup: Schematic drawing **a**) and photograph **b**)

1 to 500 kHz. The laser has a maximum average power (P_m) of 22 W and maximum pulse energy (E_{pm}) of 880 µJ before the optical system. P_m was measured after the beam expander with an Ophir laser power meter system, using a *30A-N-SH ROHS* head and *Nova II display* software. The power measurements were taken for 60 s. Maximum pulse energy was estimated with the Eq. 3 [42, 43].

$$E_{pm} = \frac{P_m}{PRF} \qquad (3)$$

The beam expander was set to give a raw laser beam diameter (D_R) of 5.7 mm. Four mirrors guide the laser beam to the scanning galvanometer mirror head fitted

with a f-theta focussing lens. This device handled the displacement of the laser beam on the sample surface and the scan rate of the laser beam (*SR*) across the surface can vary from 0.01 mm/s to 20,000 mm/s. The lens had a focal length (*FL*) of 100 mm. The samples were placed on the three axes automatic table.

In this study, the laser is used in pulsed mode with $\tau = 200$ ns, *PRF* = 25 kHz and with straight line scanning. The laser beam was focused on the sample surface. Theoretical laser beam diameter ($d_{o(Theo)}$) was around 51 μm, calculated using Eq. 4 [31, 44–46] and the values of in Table 3 for the indicated parameters.

$$d_{o(Theo)} = \frac{4FL\lambda M^2}{\pi D_R} \tag{4}$$

The focussed laser beam was scanned across the sample surfaces at a speed to produce single pulse shots. The distance between pulses (d_t) was set to 200 μm to avoid any possible overlapping of the dimples. *SR* was 5000 mm/s using Eq. 5:

$$SR = d_t PRF \tag{5}$$

Pulse energy (E_p) was varied from 4 μJ to 614 μJ in this work. E_p were estimated using Eq. 6 [42] and the average power (P_{ave}) measurements after the galvanometer mirror scanner.

$$E_p = \frac{P_{ave}}{PRF} \tag{6}$$

Maximum E_p is lower than E_{pm} because the transmission of the system is 70%. This was measured by comparing an average power measurement of the laser beam after the focussing lens with the measurements after the beam expander outputs. The selected laser parameters for this study are summarised in Table 4.

Table 4 Selected laser parameters

Parameter	Value
Wavelength, λ (μm)	1064 ± 5
Pulse length, τ (ns)	200
TEM Mode	00
Focussing lens focal length, *FL* (mm)	100.00
Raw beam diameter, D_R (mm)	5.7
Beam quality factor, M^2	2.1
Scan rate, *SR* (mm/s)	5000
Distance between pulses, d_t (μm)	200
Theoretical focus beam size, $d_{(Theo)}$ (μm)	≈ 51
Pulse Repetition Frequency, *PRF* (kHz)	25
Atmosphere	Air
Number of pulses per shot (*N*)	1
Pulse Energy, E_p (μJ)	4, 53, 108, 182, 250, 323, 402, 475, 554 and 614

Characterisation and Analysis of Dimple Dimensions

The dimensions of the dimples were assessed using an *Olympus BH2-UMA optical light microscope*, equipped with *DinoCapture 2.0* software. The topography and geometry of the dimples were evaluated with the *Bruker ContourGT optical profiler.* Assessment of the optical profilometry was conducted with green light and at $27.5\times$ magnification. The dimple shape features (e.g. width, diameter and depth) were calculated via the measuring of five dimples. Two measurements were carried out for each dimple and therefore, ten measurements for each experimental condition were conducted. It is noted that S_a measurements were not taken for the dimples, because this is not the object of this work.

Results and Discussion

Surface Morphology

The optical light microscopy pictures of the untextured (Fig. 2.a), d), g), j) and m)) and textured (Fig. 2.b-c), e–f), h-i), k-l) and n–o)) surfaces can be observed in Fig. 2. Laser impacts at ≥ 53 µJ produced textures on all samples. These show a circular shape with micro ripples in the centre and surrounded by crests. The type of textures was classified as dimples. Melting and evaporation of the material are usually the thermodynamic mechanisms that generate dimples on metals for laser irradiation with infrared laser pulses [47]. Material melting commonly creates the ablation mechanism of hydrodynamic expansion for nanosecond pulse lasers. This ablation mechanism is characterised by the displacement of molten material to edge of the laser impacted area. This displacement generates ripples and molten material massing on the edge of the dimples to create the crests [48–51]. These structures remain after the laser pulse owing to the quick temperature changes of the laser shot area. The temperature of the metallic material is quickly increased during the laser pulse. After the laser pulse impact, the temperature of the laser impacted area of the alloy is rapidly reduced by heat diffusion into the material bulk. This rapid solidification retains the ripples and crest of the dimples [33, 52]. Two dissimilar types of dimples were found, according to S_a and E_p. The first type of dimple (Fig. 2.b), e), h), k) and n)) are featured by smooth crests while the second dimple kind (Fig. 2.c), f), i), l) and o)) are characterised by an abrupt crest and molten material appearing outside of the laser exposed zone. This indicates that the ablation mechanisms of the textures were different for each type of dimple. The ablation mechanism of the first dimple kind is surface vaporisation that is featured by the conversion of liquid to gas in a liquid–gas interface that is usually named the Knudsen layer. Although the escape speed distribution of the gas material in the liquid layer initially is non-equilibrium, this distribution reaches equilibrium with time [47, 48, 53, 54]. The second type of dimple was produced by the ablation mechanism often called phase explosion, characterised by the creation and subsequent growth of a bubble that is formed of evaporated material surrounded by molten material. Gas material then presses on the molten material that when the pressure is sufficiently high, the bubble can
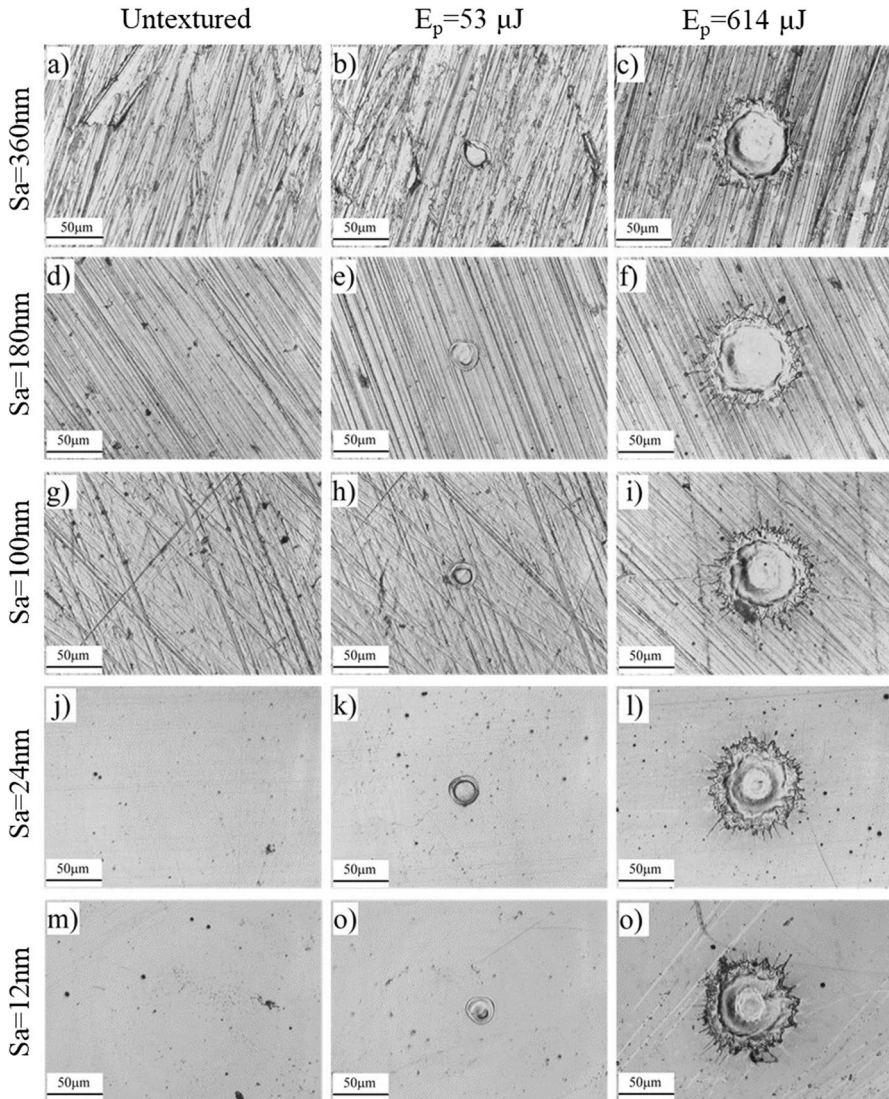
Fig. 2 The micrographic pictures of the untextured **a**), **d**), **g**), **j**) and m) surface and dimples at 53 μJ **b**), **e**), **h**), **k**) and **n**) and at 614 μJ **c**), **f**), **i**), **l**) and **o**) of the 360 nm **a-c**), 180 nm **d-f**), 100 nm **g-i**), 24 nm **j-l** and 12 nm **m–o**) samples

explode. Explosion ejects the liquid material outside of the laser treated area [47, 48, 53–58]. The first dimple type was furthermore found at lower E_p than the second dimple kind as the phase explosion requires higher energy fluence to be produced than surface vaporisation for the nanosecond pulsed lasers [47].

Dimple kinds were found at dissimilar E_p ranges for each sample. 360 nm (Fig. 2.a-c) and 180 nm (Fig. 2.d-f) samples have dimples of the first kind (Fig. 2.b and Fig. 2.e)

at $E_p \leq 475$ μJ while dimples produced by phase explosion (Fig. 2.b and Fig. 2.e) were created at $E_p \geq 554$ μJ for these surfaces. In the case of the 100 nm surface (Fig. 2.g-i), the surface vaporisation dimple (Fig. 2.h) was generated at $E_p \leq 250$ μJ and the second dimple kind (Fig. 2.i) was found at $E_p \geq 323$ μJ. For the 24 nm (Fig. 2.j-l) and 12 nm (Fig. 2.m–o) samples, the laser shots at $E^p \leq 323$ μJ produced dimples by mean of the surface vaporisation whilst phase explosion dimples were produced at $E_p \geq 402$ μJ. This showed that the roughness of the original surface has an influence on the laser energy fluence absorbed by surface. The surface with $S_a \geq 180$ nm needed higher E_p than surfaces with lower roughness because of the scattering effect of the high roughness. This effect enlarges the laser beam effective area, which reduces the energy fluence [36]. Note that the intrinsic laser parameter to determine one or other ablation mechanism is energy fluence. The phase explosion ablation mechanism is therefore produced at higher energy fluence than surface vaporisation. Phase explosion dimples were generated at lower E_p for 120 nm samples than that for 24 nm and 12 nm samples as a result of the differences in the respective samples' laser reflectivity. The reflectivity of metallic materials is inversely proportional to the surface roughness because the surface relief can cause the laser radiation to reflect at angles than the nominal incident angle of 90° [33]. The reflected laser radiation away from the normal can impact again within the laser shot area, increasing the laser radiation absorbed by the material. So, a certain roughness can be beneficial to laser absorption by metallic alloys [33]. These results indicate the existence of an optimal roughness surface for LST. An excessive roughness causes a reduction of the energy fluence while a smooth surface provokes a E_p reduction. The assessments of the laser beam-material interaction factors were carried out to confirm this assertion, this will be discussed later. Dimples on the surface with a S_a of 360 nm (Fig. 2.b-c) and 180 nm (Fig. 2.e–f) have an irregular circular shape due to the high surface roughness. The scattering effect of the roughness on the focussed laser beam causes a laser beam profile deformation that reduces the quality of the dimples [36].

The influences of the pulse energy, E_p, on the dimple width (Fig. 3.a-b) and average surface roughness, S_a, on the laser beam-material factors (Fig. 3.c-d), can be seen in Fig. 3. The width of the dimples (W), defined as the diameter of all the area processed by the laser pulse (ablation area and crest), was widened with increasing E_p, as can be in the graph of Fig. 3.a. This is due to the energy spatial distribution which is near Gaussian [45]. The dimples were wider on the surfaces with lower S_a than on the higher S_a. This can indicate that the scattering effect of the roughness is stronger than the reflectivity effect of the smooth surfaces on the LST dimple creation. The increase of laser effective area by the roughness scattering effect decreases the energy fluence. This implies that the laser beam area that can melt the metallic material is reduced [33]. This in turns causes the reduction of the dimple width with the increase of the surface roughness.

The laser beam-material factors were calculated using Eqs. 7 and 8 [34, 45, 46, 59, 60] and the linear regression method in the graph data of Fig. 3.b.

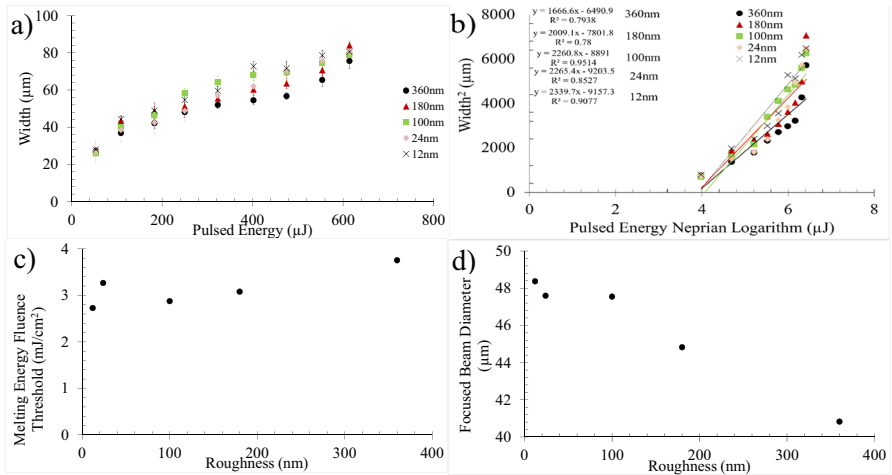$$W^2 = d_{o-m}^2 \ln(E_p) - d_{o-m}^2 \ln(E_{th-m}) \tag{7}$$

Fig. 3 Pulse energy influence on width, **a**) width as function pulse energy and **b**) width square vs pulse energy natural logarithm according to S_a and graphs of the S_a influence on the $\varphi_{th(melting)}$ **c**) and $d_{o(Theo)}$ **d**)

$$\varphi_{th-m} = \frac{4E_{th-m}}{\pi d_o^2} \qquad (8)$$

where, d_{o-m} is the experimentally determined focused laser beam diameter from the optical light microscopy data, E_{th-m} is the experimental energy threshold for melting process and φ_{th-m} is the fluence energy threshold for the melting process. The smooth surfaces typically showed lower φ_{th-m} than higher roughness surfaces (Fig. 3.c). This indicates that the polished surface at low roughness has the most efficient laser absorption than the surface with high S_a. This is due to the reduction of the roughness effect on effective laser diameter enlargement [36]. The exception is the surface at 24 nm S_a that has a higher φ_{th-m} than that for the samples with S_a of 100 nm and 180 nm. This φ_{th-m} increase is due to the reflectivity effect that decreases the laser radiation absorbed by material [61]. This effect is attenuated by hydrodynamic expansion for the 12 nm samples. The low surface roughness can, moreover, result in the low resistance of the surface to the flow of molten material across the surface. This hydrodynamic expansion produces the movement of the liquid material outside of the laser impacted area [47]. This movement on the surface can be limited by surface relief that is proportional to S_a. These results also show that the roughness scattering effect on laser beam-material interactions is the predominant surface parameter at $S_a \geq 100$ nm while the laser radiation reflection is the dominant factor for surfaces at $S_a \leq 24$ nm. The melting fluence energy, φ_{th-m}, of the samples were slightly higher than the theoretical melting energy fluence (φ_{Theo-m}) whose value is 2.625 J/cm^2, calculated using Table 2 data and Eq. 9 [26, 62, 63]. The slight difference with the samples at high roughness is due the roughness scattering effect [34].

$$\varphi_{th(Theo-m)} = \frac{\rho\big(C_p\big(T_m - T_o\big) + \Delta H_m\big)}{1 - R}\left(\sqrt{\kappa\tau} + \frac{1}{\alpha}\right) \qquad (9)$$

d_{o-m} of the samples (Fig. 3.c) increased as S_a is reduced because it is the focused laser beam area that can melt the SS316L. The laser beam has an energy spatial distribution close to Gaussian. Maximum fluence is in the centre of the laser spot and reduces towards the edge of the spot, so the laser spot centre can melt the material while the laser beam edge can only heat the material [30]. The surface roughness enlarges the laser beam diameter by means of laser scattering [36]. This enlargement of the laser beam diameter decreases energy fluence and therefore, the melted surface area is reduced. Although the calculated d_{o-m} of the samples varied, all diameters were only a 20% maximum deviation from $d_{o(Theo)}$ (51 µm), which is reasonable.

Topography

Dimples have different topographies according to the values of S_a and E_p, as can be seen in Fig. 4 (3D pictures) and Fig. 5 (Profile images). Dimples mainly have a shape that consists of a depression surrounded by a crest. The depression is generated by the ablation of the material through the evaporation of the material and the movement and ejection of the molten material to the outside of the laser shot area [64, 65], as mentioned in *3.1. Surface Morphology*. The dimple form has a spherical cap. These dimples are therefore classified as U-type [66–69]. This geometry arises as the Gaussian peak of the laser beam possesses sufficient energy to ablate the metallic material [31, 69, 70]. Dimples with a different shape were found at $E_p = 53$ µJ for surfaces with 12 nm of S_a, (Fig. 4.n and Fig. 5.e). These dimples are formed of a peak in the centre of the laser impacted area that was surrounded by a valley that is, in-turn, surrounded by a crest. These dimples are classified according to their shape as "sombrero" type [31, 33, 71]. This kind of dimple is produced by the Marangoni effect that causes the movement of the liquid material to the edge and centre of the laser exposure point. This effect is caused by the thermal gradient differences in the liquid metal pool. The effect is found for the laser treatments where the melting is the dominant thermal process [31, 33]. This indicates that the 12 nm samples absorbed less laser radiation than other surfaces because melting needs less energy fluence than evaporation [47].

The crest of the dimples created by the ablation mechanism of phase explosion (Fig. 4.c, f, i, l and o) were wider and higher than the crest caused by surface vaporisation. Evaporated material pressure on the molten metal displaces the liquid material to edge of the dimple [10, 47, 65]. This increases the size of the crest. This pressure is considerable for the phase explosion owing to the confinement of the gas material into the bubble of the phase explosion [47, 72].

The quality of the dimple shape was better for the samples with smooth surface because the low relief (Fig. 5.a higher relief and Fig. 5.d low relief). Peaks and valleys of the non-textured surface cause the absorption of the laser radiation to be heterogeneous. This alters the Gaussian like shape of the laser beam as it is exposed on
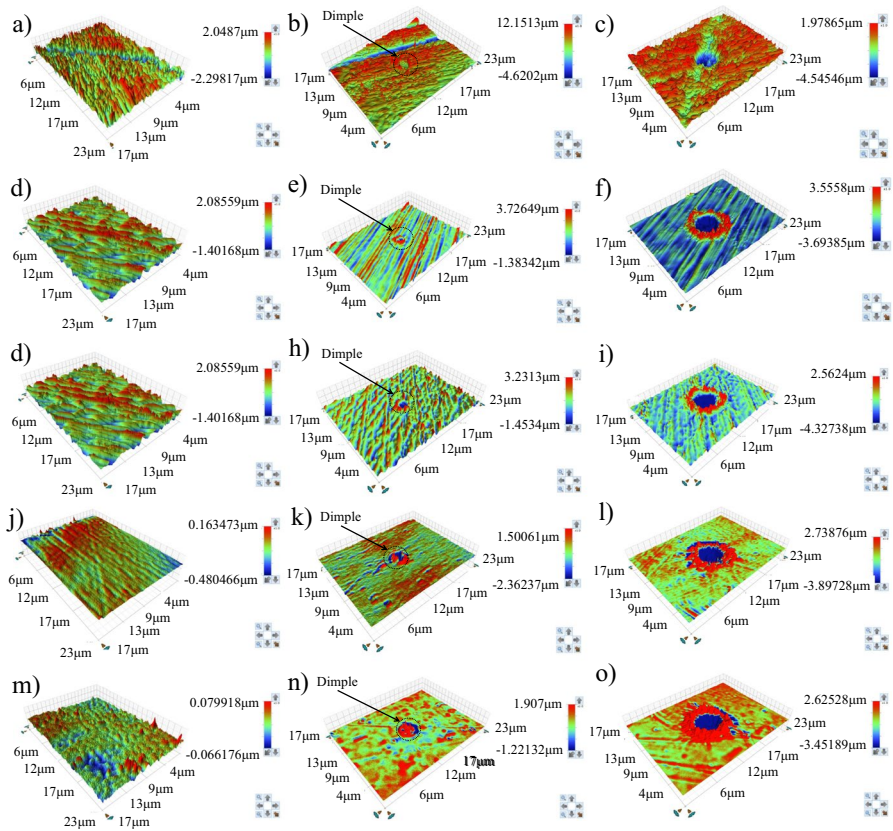
Fig. 4. 3D images of the untextured **a**), **d**), **g**), **j**) and **m**) surface and dimples at 53 μJ **b**), **e**), **h**), **k**) and **n**) and at 614 μJ **c**), **f**), **i**), **l**) and **o**) of the 360 nm **a-c**), 180 nm **d-f**), 100 nm **g-i**) 24 nm **j-l**) and 12 nm **m–o**) samples

to the metallic surface [30]. The roughness scattering effect on the laser radiation can also modify the shape of the dimples [36].

The diameter of the dimples (d) is a texture feature that is defined as the diameter of the laser ablated area (laser exposure area without crest). Figure 6 shows the influence of E_p on dimple diameter and S_a on the laser beam-material interaction.

The diameter increased with E_p (Fig. 6.a) as the laser beam has a Gaussian energy spatial distribution [9, 69]. d was higher on surface with low S_a because of the laser scattering effect of the surface relief [36]. d_{o-a} (focused laser beam diameter) and E_{th-sa} (minimum laser energy to ablate the surface) were calculated using Eq. 10 [9, 34, 41, 56, 73] while φ_{th-sa} (minimum laser energy fluence to ablate the surface) was estimated with Eq. 7 but with d_{o-m} and E_{th-m} replaced by d_{o-a} and E_{th-sa}.

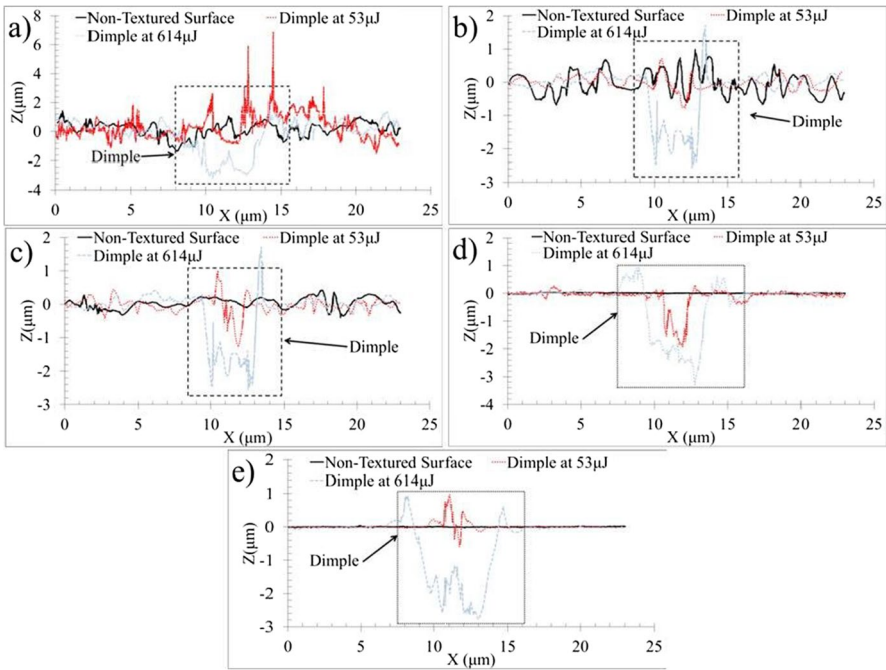$$d^2 = d_{o-a}^2 \ln(E_p) - d_{o-a}^2 \ln(E_{th-sa}) \tag{10}$$

Fig. 5 Profile images of the untextured surface and the dimples at 53 μJ and at 614 μJ of the 360 nm **a**), 180 nm **b**), 100 nm **c**), 24 nm **d**) and 12 nm **e**) samples
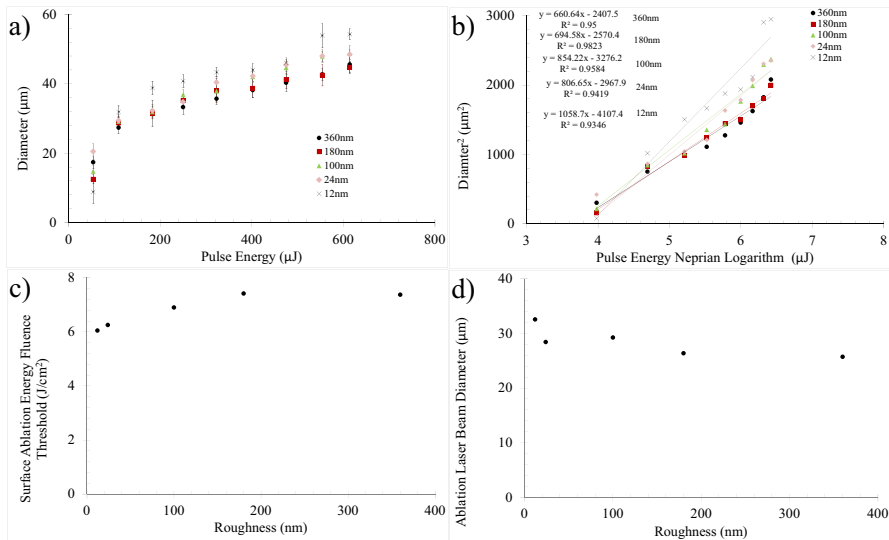

Fig. 6 Pulse energy influence on the dimple diameter of the samples, **a**) diameter as function of pulse energy, **b**) diameter squared vs pulse energy natural logarithm, **c**) surface ablation energy fluence threshold vs pulse energy and **d**) ablation laser beam diameter against S_a

The linear regression used to estimate φ_{th-sa} and d_{o-a} can be seen in Fig. 6.b. φ_{th-sa} decreases with the reduction of the surface roughness as can be observed in Fig. 6.c. This seems to show that the laser scattering effect of the roughness is more predominant than the reflectivity effect for this roughness (from 12 to 360 nm). φ_{th-sa} of the samples (≈ 7 J/cm^2) was lower than the theoretical ablation fluence threshold $\varphi_{th(Theo-e)}$ (11.168 J/cm^2) that was calculated using Eq. 11 [26, 31, 58, 62, 74, 75]:

$$\varphi_{th(Theo-e)} = \frac{\rho\left(C_p\left(T_e - T_m\right) + \Delta H_e + C_p\left(T_m - T_o\right) + \Delta H_m\right)}{1 - R}\left(\sqrt{\kappa\tau} + \frac{1}{\alpha}\right)$$

(11)

This is due to the explosive phase producing extra ablation material than the simple vaporising of the material. The explosion of the bubble provokes an increase of the amount of removed material owing to the ejection of the molten material, which is typical of the phase explosion [55]. φ_{th-sa} was higher than φ_{th-m} for all samples as the required energy to vaporise the material is larger than that for melting [30, 47].

d_{o-a} increases with the decrease of S_a, as can be seen in Fig. 6.d. This is as a result of the reduction of laser effective area with rising S_a [34]. This in turn causes the energy fluence to be higher for surfaces with low surface roughness and therefore, wider laser beam areas can be evaporated on the material.

d_{o-a} of the samples (≈ 30 μm) are smaller than $d_{o(Theo)}$ (51 μm) because of the Gaussian like profile. Only the central areas of the laser beam can ablate the material, so, d_{o-a} is lower than d_{o-m} due to the higher energy fluence required for vaporising process than melting [30].

The influence of E_p and S_a on the depth of the dimples and the depth related laser-material interactions can be found in Fig. 7. All U-type dimples were deep while the sombrero-like dimples had raised central point (dimples on 12 nm surface at 53 μJ). These sombrero-like dimples were excluded from the analysis of S_a and E_p influence on dimple depth (De). An increase in E_p deepens the dimples for all surface roughnesses (Fig. 7.a) as the rate of ablation is proportional to this laser parameter [64]. The samples with lower S_a commonly have deeper dimples than the samples with high S_a. This is due to the reduction of the roughness scattering effect with decreasing S_a [36]. The two exceptions were the dimples on $S_a = 360$ nm samples that were deeper than that for samples with lower roughness, and $S_a = 12$ nm sample dimples that were shallower than the $S_a = 24$ nm sample dimples. In the case of the $S_a = 360$ nm sample dimples, this can be due to the large relief of the original surface. On such surfaces, the difference of the height between the original surface peaks and valleys can reach 3 μm. This height can be of the same scale as the depth of the dimples for this surface. Thus, the depth of the dimples for the $S_a = 360$ nm samples were greater than for those samples with low S_a. For the $S_a = 12$ nm sample dimples. The explanation is the high reflectivity of the smooth surfaces [47].

Energy depth penetration (l) (the depth to which absorbed laser energy is transferred into the material) and pulse energy threshold (E_{th-da}) (necessary minimum pulse energy to create a dimple with visible depth) were calculated using the graph of Fig. 7.b. (linear regressions) and Eq. 12 [26, 60, 64, 74].
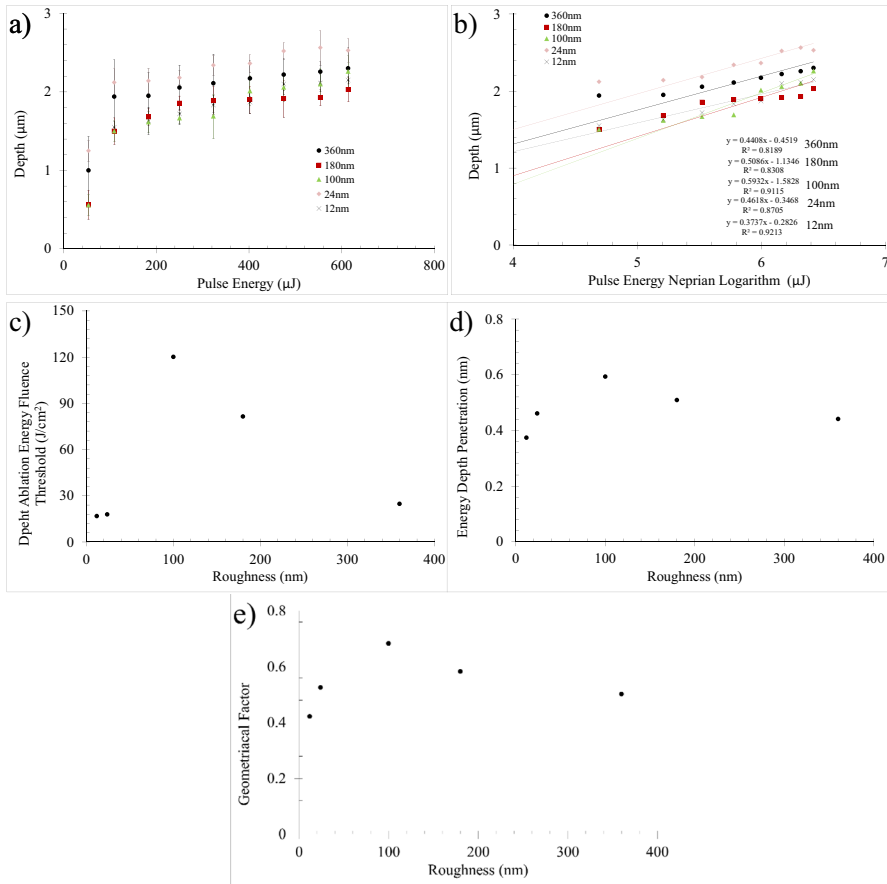
Fig. 7 Pulse energy on dimple depth of the samples, **a**) depth as function pulse energy, **b**) depth vs pulse energy natural logarithm, **c**) depth ablation energy fluence threshold against roughness, **d**) energy depth penetration vs. roughness and **e**) geometrical factor on function to roughness

$$De = l\ln\left(E_p\right) - l\ln(E_{th-da}) \tag{12}$$

Depth ablation energy fluence (φ_{th-da}) were estimated with Eq. 8 but the d_{o-m} and E_{th-m} are replaced by d_{o-a} and E_{th-da}. This was carried out to have an intrinsic and comparable value between samples. φ_{th-da} of all samples (Fig. 7.c) were higher than all φ_{th-sa} and φ_{th-e}, which can indicate the micro plasma generation at the bottom of the dimple. The evaporated material can interact with the laser radiation, which increases the temperature of the gas. If the material in gas state reaches a certain temperature, this can convert to plasma that can absorb, reflect, and scatter the laser radiation. This can diminish the laser energy absorbed by the material. The plasma effect on the laser radiation is often called the "plasma shielding effect" [48, 72, 76–78]. It is noted that plasma can take from 10 ps to a few ns to form [77] and therefore, this can be produced during the laser pulse (200 ns pulse length). Plasma is only created in the centre of the

dimple due to the high energy fluence that can be found in the centre of the laser spot [48]. φ_{th-da} was increased with reducing S_a until $S_a = 180$ nm. This is as a result of the reduction in the roughness laser scattering effect that decreases the laser effective area [34]. This in turns enlarges the effective energy fluence. The temperature of the plasma is proportional to laser energy fluence and the plasma time generation is inversely proportional to this laser parameter. Plasma absorptivity is proportional to the increase in plasma temperature [72]. The smoother surface therefore produces a stronger plasma shielding effect than rougher surfaces up to $S_a = 24$ nm. φ_{th-da} of the $S_a = 24$ nm and $S_a = 12$ nm samples were lower than that for other samples due to the reflectivity effect. Part of the laser radiation is reflected by the metallic material, which decreases the laser energy absorbed by material [79]. This decreases the amount of the evaporated material that in turns reduces the density of the plasma. The plasma shielding effect is proportional to its density [48, 72, 76, 77]. Thus, the plasma shielding effect is weakened. So, the laser radiation absorbed by the material is increased as a result of the reduction of the plasma shielding effect. Note that the plasma shielding effect was absent in the case of the surface features (melt and ablation widths / diameters) because the plasma was only produced on bottom of the dimple. The $S_a = 24$ nm (18 J/cm^2) and $S_a = 12$ nm (17 J/cm^2) sample φ_{th-da} were higher than φ_{th-e} (11.168 J/cm^2) as the plasma shielding effect still had influence on the laser radiation observed [72].

The influence of S_a on energy depth penetration, l, is similar to the case of φ_{th-da} as can be seen in Fig. 7.d. This can indicate that the l is influenced by the same processes as φ_{th-da}. The value of this factor is lower than theoretical energy depth penetration l_{Theo} (858 nm) that is calculated using Eq. 13 [31, 45, 57, 80, 81] and the data in Table 2.

$$l_{Theo} = \sqrt{\tau \kappa} + \frac{1}{\alpha} \qquad (13)$$

This difference can be quantified through the geometrical factor (ζ) that is estimated using the Eq. 14 [31, 45, 80]. It is noted that the influence of α on l_{Theo} is minimum for nanosecond pulsed laser texturing on metallic materials.

$$\zeta = \frac{\sqrt{l - \frac{1}{\alpha}}}{\tau \kappa} \qquad (14)$$

Figure 7e shows that the $S_a = 100$ nm samples have the best surface to absorb the laser radiation in depth as this surface has ζ nearest to one (≈ 0.7). An excessive roughness can produce a heterogeneous absorption of the laser in depth that decreases the effectiveness of this process [34] while an extremely smooth surface causes a reflectivity effect that diminishes the laser radiation absorbed by the material [61].

Conclusions

The present study shows that the effect of the original surface roughness on laser surface texturing in the form of individual dimples. The dimples are generated via two ablation mechanisms: normal evaporation at low energy and phase explosion

at high fluence. Initial surface roughness has differing influences according to the dimple features. The quality of the shape of the dimples is improved with the reduction in the surface roughness while more energetic ablation mechanisms were found at lower pulse energy for the 100 nm samples. Two types of dimples can be created with the correct combination of laser parameter and surface roughness. The U-type dimple is the more common kind, while the sombrero-like type dimple is produced at minimum pulse energy (53 μJ) on $S_a = 12$ nm samples. The increase of the dimple width requires less pulse energy for the smooth surfaces ($S_a = 12$ nm) than for rough surfaces. Dimples are deepened easier on $S_a = 24$ nm samples than other samples. The highest energy depth penetration is found for the $S_a = 100$ nm sample. This difference between the surface laser texturing processes with depth is due to the generation of the plasma shielding effect at the bottom of the dimple, which only affects the dimple depth.

According to the outcomes of this study, the following recommendation can be made about the surface for laser surface texturing. The optimum surface to produce wide dimples is the surface at $S_a = 12$ nm while the deepest dimples are easier to create on polished surfaces with $S_a = 24$ nm. The samples at $S_a = 100$ nm are a suitable surface to fabricate phase explosion dimples with large energy depth penetration value.

This information can help to improve the efficiency of laser surface texturing process on SS316L, which can reduce the cost of the process to industry. This study also indicates how to generate different types of dimples and design their features.

Declarations

References

1. Molak, R.M., Paradowski, K., Brynk, T., Ciupinski, L., Pakiela, Z., Kurzydlowski, K.J.: Measurement of mechanical properties in a 316L stainless steel welded joint. Int. J. Press. Vessels Pip. **86**(1), 43–47 (2009)
2. Kedia, S., Bonagani, S.K., Majumdar, A.G., Kain, V., Subramanian, M., Maiti, N., Nilaya, J.P.: Nanosecond laser surface texturing of type 316L stainless steel for contact guidance of bone cells and superior corrosion resistance. Colloid Interf. Sci. Commun. **42**, 100419 (2021)
3. Lin, N., Liu, Q., Zou, J., Guo, J., Li, D., Yuan, S., Ma, Y., Wang, Z., Wang, Z., Tang, B.: Surface texturing-plasma nitriding duplex treatment for improving tribological performance of AISI 316 stainless steel. Materials **9**(11), 875 (2016)
4. Rapoport, L., Moshkovich, A., Perfilyev, V., Lapsker, I., Halperin, G., Itovich, Y., Etsion, I.: Friction and wear of MoS2 films on laser textured steel surfaces. Surf. Coat. Technol. **202**(14), 3332–3340 (2008)
5. Etsion, I.: State of the art in laser surface texturing. J Trib **127**(1), 248–253 (2005)
6. Hu, T., Zhang, Y., Hu, L.: Tribological investigation of MoS2 coatings deposited on the laser textured surface. Wear **278**, 77–82 (2012)
7. Mao, B., Siddaiah, A., Liao, Y., Menezes, P.L.: Laser surface texturing and related techniques for enhancing tribological performance of engineering materials: A review. J. Manuf. Process. **53**, 153–173 (2020)
8. Nsilani, K.A., Ma, Q., Liu, Q., Mawignon, F.J., Rafique, F., Dong, G.: Design methodology and application of surface texture: A review. Coatings **12**(7), 1015 (2022)
9. Puoza, J.C., Hua, X., Liu, Q., Kang, Z., Zhang, P.: Manufacturing of micro-textures on metals by nanosecond laser micromachining. Adv. Mater. Process. Technol. **4**(1), 86–99 (2018)
10. Cha, D., Axinte, D., Billingham, J.: Geometrical modelling of pulsed laser ablation of high performance metallic alloys. Int. J. Mach. Tools Manuf **141**, 78–88 (2019)
11. Knowles, M., Rutterford, G., Karnakis, D., Ferguson, A.: Micro-machining of metals, ceramics and polymers using nanosecond lasers. Int. J. Adv. Manuf. Technol. **33**(1), 95–102 (2007)
12. Etsion, I.: State of the art in laser surface texturing. Eng. Syst. Design Anal. **41731**, 585–593 (2004)
13. Baharin, A.F.S., Ghazali, M.J., Wahab, J.A.: Laser surface texturing and its contribution to friction and wear reduction: a brief review. Indust. Lubr. Tribol. **68**(1) (2016)
14. Wahab, J., Ghazali, M., Yusoff, W., Sajuri, Z.: Enhancing material performance through laser surface texturing: A review. Transact. IMF **94**(4), 193–198 (2016)
15. De Zanet, A., Casalegno, V., Salvo, M.: Laser surface texturing of ceramics and ceramic composite materials–A review. Ceram. Int. **47**(6), 7307–7320 (2021)
16. Bathe, R., Padmanabham, G., Thirumalini, S., Vaira, Vignesh R.: Impact of laser surface texturing (LST) on the tribological characteristics of piston rings and cylinder liners–a review. Part 1: development of LST technology. Transact. IMF **99**(5), 231–237 (2021)
17. Sirdeshmukh, N., Dongre, G.: Laser micro & nano surface texturing for enhancing osseointegration and antimicrobial effect of biomaterials: A review. Mater. Today: Proc. **44**, 2348–2355 (2021)
18. Riveiro, A., Maçon, A.L., del Val, J., Comesaña, R., Pou, J.: Laser surface texturing of polymers for biomedical applications. Front. Phys. **6**, 16 (2018)
19. Shivakoti, I., Kibria, G., Cep, R., Pradhan, B.B., Sharma, A.: Laser surface texturing for biomedical applications: a review. Coatings **11**(2), 124 (2021)
20. Han, J., Zhang, F., Van Meerbeek, B., Vleugels, J., Braem, A., Castagne, S.: Laser surface texturing of zirconia-based ceramics for dental applications: A review. Mater. Sci. Eng., C **123**, 112034 (2021)
21. Barosz, P., Gołda, G., Kampa, A.: Efficiency analysis of manufacturing line with industrial robots and human operators. Appl. Sci. **10**(8), 2862 (2020)
22. Eichhammer, W., Wilhelm, M.: Industrial energy efficiency: indicators for a European cross-country comparison of energy efficiency in the manufacturing industry. Energy Policy **25**(7–9), 759–772 (1997)
23. Apostolos, F., Alexios, P., Georgios, P., Panagiotis, S., George, C.: Energy efficiency of manufacturing processes: a critical review. Procedia Cirp **7**, 628–633 (2013)
24. Matilainen, V., Piili, H., Salminen, A., Syvänen, T., Nyrhilä, O.: Characterization of process efficiency improvement in laser additive manufacturing. Phys. Procedia **56**, 317–326 (2014)

25. Domke, M., Matylitsky, V., Stroj, S.: Surface ablation efficiency and quality of fs lasers in single-pulse mode, fs lasers in burst mode, and ns lasers. Appl. Surf. Sci. **505**, 144594 (2020)
26. Wu, B., Liu, P., Wang, X., Zhang, F., Deng, L., Duan, J., Zeng, X.: Effect of laser absorption on picosecond laser ablation of Cr12MoV mold steel, 9Cr18 stainless steel and H13A cemented carbide. Opt. Laser Technol. **101**, 11–20 (2018)
27. Schneider, J., Braun, D., Greiner, C.: Laser textured surfaces for mixed lubrication: influence of aspect ratio, textured area and dimple arrangement. Lubricants **5**(3), 32 (2017)
28. Neuenschwander, B., Jaeggi, B., Schmid, M., Dommann, A., Neels, A., Bandi, T., Hennig, G.: Factors controlling the incubation in the application of ps laser pulses on copper and iron surfaces. In: Laser Applications in Microelectronic and Optoelectronic Manufacturing (LAMOM) XVIII, 2013. SPIE **86070D**, 26–35 (2013)
29. Li, Q., Perrie, W., Potter, R., Allegre, O., Li, Z., Tang, Y., Zhu, G., Liu, D., Chalker, P., Ho, J.: Femtosecond laser micro-structuring of amorphous polyether (ether) ketone at 775 nm and 387 nm. J. Phys. D Appl. Phys. **53**(36), 365301 (2020)
30. Cheng, J., Perrie, W., Sharp, M., Edwardson, S., Semaltianos, N., Dearden, G., Watkins, K.: Single-pulse drilling study on Au, Al and Ti alloy by using a picosecond laser. Appl. Phys. A **95**(3), 739–746 (2009)
31. Wlodarczyk, K.L., Ardron, M., Waddie, A.J., Dunn, A., Kidd, M.D., Weston, N.J., Hand, D.P.: Laser microsculpting for the generation of robust diffractive security markings on the surface of metals. J. Mater. Process. Technol. **222**, 206–218 (2015)
32. Wang, S., Yan, F., Chen, A.: Tribological effects of laser surface texturing and residual stress. Industr. Lubric. Tribol. **70**(1) (2018)
33. Brown, M.S., Arnold, C.B.: Fundamentals of laser-material interaction and application to multiscale surface modification. In: Laser precision microfabrication. Springer, **135**, 91–120 (2010)
34. Mustafa, H., Mezera, M., Matthews, D.T.A., Römer, G.: Effect of surface roughness on the ultrashort pulsed laser ablation fluence threshold of zinc and steel. Appl. Surf. Sci. **488**, 10–21 (2019)
35. Auinger, M., Ebbinghaus, P., Blümich A., Erbe, A.: Effect of surface roughness on optical heating of metals. J. Eur. Optical Soc.-Rapid Public. **9**(14004) (2014)
36. House, R., Bettis, J., Guenther, A.: Surface roughness and laser damage threshold. IEEE J. Quantum Electron. **13**(5), 361–363 (1977)
37. Kim, C.S.: Thermophysical properties of stainless steels. Argonne National Lab., Illinois (1975)
38. Yan, J., Zhou, Y., Gu, R., Zhang, X., Quach, W.-M., Yan, M.: A comprehensive study of steel powders (316L, H13, P20 and 18Ni300) for their selective laser melting additive manufacturing. Metals **9**(1), 86 (2019)
39. Faucon M., Laffitte A., Lopez J., Kling R. Surface blackening by laser texturing with high repetition rate femtosecond laser up to 1MHz. In: Frontiers in Ultrafast Optics: Biomedical, Scientific, and Industrial Applications XIV, 2014. SPIE **89721M**, 256–263 (2014)
40. Zhou, J., Shen, H., Pan, Y., Ding, X.: Experimental study on laser microstructures using long pulse. Opt. Lasers Eng. **78**, 113–120 (2016)
41. Wang, Y., Zhang, M., Huang, Y., Cao, X., Dong, Y., Zhao, J., Li, Y., Wang, Y.: Ablation threshold modelling and validation of metal Nanosecond laser processing. Optics Commun. **523**, 128608 (2022)
42. Jiang, D., Alsagri, A.S., Akbari, M., Afrand, M., Alrobaian, A.A.: Numerical and experimental studies on the effect of varied beam diameter, average power and pulse energy in Nd: YAG laser welding of Ti6Al4V. Infrared Phys. Technol. **101**, 180–188 (2019)
43. Coroado, J., Ganguly, S., Suder, W., Williams, S., Meco, S., Pardal, G.: Selection of parameters in nanosecond pulsed wave laser micro-welding. Int. J. Adv. Manuf. Technol. **115**(9), 2929–2944 (2021)
44. Sola, D., Conde, A., García, I., Gracia-Escosa, E., De Damborenea, J.J., Peña, J.I.: Microstructural and wear behavior characterization of porous layers produced by pulsed laser irradiation in glass-ceramics substrates. Materials **6**(9), 3963–3977 (2013)
45. Mannion, P., Magee, J., Coyne, E., O'connor, G., Glynn, T.: The effect of damage accumulation behaviour on ablation thresholds and damage morphology in ultrafast laser micro-machining of common metals in air. Appl. Surf. Sci. **233**(1–4), 275–287 (2004)
46. Convert, L., Bourillot, E., François, M., Pocholle, N., Baras, F., Politano, O., Costil, S.: Laser textured titanium surface characterization. Appl. Surf. Sci. **586**, 152807 (2022)
47. Wu B., Özel T.: Micro-Laser Processing. Micro-Manufacturing: Design and Manufacturing of Micro-Products:159–195. (2011)

48. Marla, D., Bhandarkar, U.V., Joshi, S.S.: A model of laser ablation with temperature-dependent material properties, vaporization, phase explosion and plasma shielding. Appl. Phys. A **116**(1), 273–285 (2014)

49 Williams, E., Brousseau, E.: Nanosecond laser processing of Zr41. 2Ti13. 8Cu12. 5Ni10Be22. 5 with single pulses. J. Mater. Process. Technol. **232**, 34–42 (2016)

50. Zhu, Y., Fu, J., Zheng, C., Ji, Z.: Effect of nanosecond pulse laser ablation on the surface morphology of Zr-based metallic glass. Opt. Laser Technol. **83**, 21–27 (2016)

51. Zhao, J., Zhu, Z., Xu, Y., Song, X., Wang, Y., Peng, H., Wang, Y., Zuo, J., Shu, X., Yin, A.: Nanosecond Laser Ablation of Ti–6Al–4V under Different Temperature. Appl. Sci. **10**(13), 4657 (2020)

52. Pou-Álvarez, P., Riveiro, A., Nóvoa, X., Fernández-Arias, M., del Val, J., Comesaña, R., Boutinguiza, M., Lusquiños, F., Pou, J.: Nanosecond, picosecond and femtosecond laser surface treatment of magnesium alloy: role of pulse length. Surf. Coat. Technol. **427**, 127802 (2021)

53. Wang, Y., Shen, H., Liu, C., Hou, X., Tan, Y., Hao, Z., Li, C.: Evolution of nanosecond laser-induced phase explosion based on a high-speed continuous imaging system. Results Phys. **29**, 104782 (2021)

54. Guo, L., Li, Y., Geng, S., Wang, C., Jiang, P.: Numerical and experimental analysis for morphology evolution of 6061 aluminum alloy during nanosecond pulsed laser cleaning. Surf. Coat. Technol. **432**, 128056 (2022)

55. Song, K.H., Xu, X.: Explosive phase transformation in excimer laser ablation. Appl. Surf. Sci. **127**, 111–116 (1998)

56. Chen, M., Wang, X., Qi, D., Deng, H., Liu, Y., Shen, X.: Temperature field simulation of chalcogenide glass ablation by nanosecond pulsed laser-based on pump–probe technology. Opt. Laser Technol. **149**, 107771 (2022)

57. Sinha, S.: Laser based surface treatment of bioactive glass: Dependence on pulsed laser ablation. Appl. Surf. Sci. Adv. **11**, 100295 (2022)

58. Grabowski, A., Florian, T., Wieczorek, J., Adamiak, M.: Structuring of the Ti6Al4V alloy surface by pulsed laser remelting. Appl. Surf. Sci. **535**, 147618 (2021)

59. Zhou, C., Li, H., Chen, G., Wang, G., Shan, Z.: Effect of single pulsed picosecond and 100 nanosecond laser cleaning on surface morphology and welding quality of aluminium alloy. Opt. Laser Technol. **127**, 106197 (2020)

60. Mustafa, H., Matthews, D.T., Römer, G.: Wavelength dependence of picosecond-pulsed laser ablation of hot-dip galvanized steel. Appl. Phys. A **128**(4), 1–18 (2022)

61. Fu, Y., Li, J., Liu, Y., Liu, L., Zhao, H., Pan, Y.: Influence of surface roughness on laser-induced damage of Nd: YAG transparent ceramics. Ceram. Int. **41**(10), 12535–12542 (2015)

62. Domke, M., Nobile, L., Rapp, S., Eiselen, S., Sotrop, J., Huber, H.P., Schmidt, M.: Understanding thin film laser ablation: The role of the effective penetration depth and the film thickness. Phys. Procedia **56**, 1007–1014 (2014)

63. Mao, Y.-Z., Yang, J.-X., Ji, J.-C.: Theoretical and experimental study of surface texturing with laser machining. Adv. Manuf. **9**(4), 538–557 (2021)

64. Ahuir-Torres, J., Arenas, M., Perrie, W., De Damborenea, J.: Influence of laser parameters in surface texturing of Ti6Al4V and AA2024-T3 alloys. Opt. Lasers Eng. **103**, 100–109 (2018)

65. Baumgart, P., Krajnovich, D., Nguyen, T., Tam, A.: A new laser texturing technique for high performance magnetic disk drives. IEEE Trans. Magn. **31**(6), 2946–2951 (1995)

66. Nanbu, T., Ren, N., Yasuda, Y., Zhu, D., Wang, Q.J.: Micro-textures in concentrated conformal-contact lubrication: effects of texture bottom shape and surface relative motion. Tribol. Lett. **29**(3), 241–252 (2008)

67. Gropper, D., Wang, L., Harvey, T.J.: Hydrodynamic lubrication of textured surfaces: a review of modeling techniques and key findings. Tribol. Int. **94**, 509–529 (2016)

68. Shiman, O., Gerbreders, V., Sledevskis, E., Paskevics, V.: Electron beam induced surface modification of amorphous Sb2Se3 thin film. J. Non-Cryst. Solids **358**(8), 1153–1156 (2012)

69. Zhan, X., Liu, Y., Yi, P., Jia, D., Xiao, P.: Study on the influence of scanning strategy on the morphology of laser micro-dimple texturing. In: Tenth International Conference on Information Optics and Photonics, 2018. International Society for Optics and Photonics, 109640P (2018)

70. Wang, Y., Zhang, M., Dong, Y., Zhao, J., Zhu, X., Li, Y., Fan, L., Leng, H.: Morphology modelling and validation in nanosecond pulsed laser ablation of metallic materials. Precis. Eng. **79**, 34–42 (2023)

71. He, Y., Yang, J., Wang, H., Gu, Z., Fu, Y.: Micro-dimple and micro-bulge textures: Influence of surface topography types on stick–slip behavior under starved lubrication. Appl. Surf. Sci. **585**, 152501 (2022)
72. Vadillo, J., Fernández, R.J., Rodriguez, C., Laserna, J.: Effect of plasma shielding on laser ablation rate of pure metals at reduced pressure. Surf. Interf. Anal. **27**(11), 1009–1015 (1999)
73. Nivas, J., Allahyari, E., Vecchione, A., Hao, Q., Amoruso, S., Wang, X.: Laser ablation and structuring of CdZnTe with femtosecond laser pulses. J. Mater. Sci. Technol. **48**, 180–185 (2020)
74. Holder, D., Weber, R., Graf, T., Onuseit, V., Brinkmeier, D., Förster, D.J., Feuer, A.: Analytical model for the depth progress of percussion drilling with ultrashort laser pulses. Appl. Phys. A **127**(5), 1–8 (2021)
75. Holder, D., Weber, R., Graf, T.: Analytical Model for the Depth Progress during Laser Micromachining of V-Shaped Grooves. Micromachines **13**(6), 870 (2022)
76. Vasantgadkar, N.A., Bhandarkar, U.V., Joshi, S.S.: A finite element model to predict the ablation depth in pulsed laser ablation. Thin Solid Films **519**(4), 1421–1430 (2010)
77. Russo, R.E., Mao, X., Yoo, J., Gonzalez, J.: Laser ablation. In: Laser-induced breakdown spectroscopy. Elsevier **2**, 41–70 (2007)
78. Lu, Y., Yang, L., Wang, M., Wang, Y.: Simulation of nanosecond laser cleaning the paint based on the thermal stress. Optik **227**, 165589 (2021)
79. Ang, L., Lau, Y., Gilgenbach, R.M., Spindler, H.: Analysis of laser absorption on a rough metal surface. Appl. Phys. Lett. **70**(6), 696–698 (1997)
80. Xiao, S., Schöps, B., Ostendorf, A.: Selective ablation of thin films by ultrashort laser pulses. Phys. Procedia **39**, 594–602 (2012)
81. Dausinger, F.: Femtosecond technology for precision manufacturing: Fundamental and technical aspects. In: Third International Symposium on Laser Precision Microfabrication, 2003. SPIE **48030**, 471–478 (2003)